Nano Research

Open Access

Research Article

Surface-defect engineering of metal nanoclusters for highly efficient electrocatalytic CO_2 reduction

Haoqi Li[1,§], Yafu Wang[2,§], Xiao Wei[1], Zhaohang Chen[1], Rui Ren[2], Xi Kang[1] ✉, Jiangwei Zhang[2] ✉, and Manzhou Zhu[1] ✉

[1] *Department of Chemistry and Centre for Atomic Engineering of Advanced Materials, Key Laboratory of Structure and Functional Regulation of Hybrid Materials of Ministry of Education, Anhui Province Key Laboratory of Chemistry for Inorganic/Organic Hybrid Functionalized Materials, Anhui University, Hefei 230601, China*

[2] *College of Energy Material and Chemistry, Inner Mongolia Key Laboratory of Low Carbon Catalysis, Inner Mongolia University; Inner Mongolia Advanced Research Institute, Ministry of Education, Hohhot 010021, China*

§ *Haoqi Li and Yafu Wang contributed equally to this work.*

Cite this article: *Nano Research*, **2026**, *19*, 94908428. https://doi.org/10.26599/NR.2026.94908428

ABSTRACT: Defect engineering serves as a pivotal strategy for improving the performance of CO_2 electrocatalytic reduction (CO_2RR). However, understanding the structure-activity relationship between defect configurations and catalytic activity at the atomic level remains a significant challenge. This study utilized a series of structurally well-defined $Au_1Ag_{24+2n}(SR)_{18+n}$ (where n = 0, 1, 2; SR = adamantanethiol) nanoclusters as model catalysts to systematically explore the impact of defect engineering on CO_2RR. In the Au_1Ag_{26} nanocluster, rearrangement of the peripheral ligands creates structural defects, which increases the exposure of the active surface area. This defect engineering leads to optimal catalytic performance, achieving a Faradaic efficiency (FE) for CO of 63% at −1.0 V (vs. RHE)—nearly double that of Au_1Ag_{24}, which has an FE of 32%. In contrast, due to the surface units of Au_1Ag_{28} being fully covered, its catalytic activity is negligible (FE_{CO} < 5%). By integrating comprehensive structural characterization with electrocatalytic performance analysis, we have demonstrated at the atomic level that the Ag_1S_3 motif acts as the possible catalytic active center, with catalytic performance exhibiting a direct correlation with the degree of active site exposure. This research uncovers the fundamental mechanism by which defect engineering enhances CO_2RR catalyst performance by reconstructing the coordination environment and strategically exposing active sites of cluster-based catalysts.

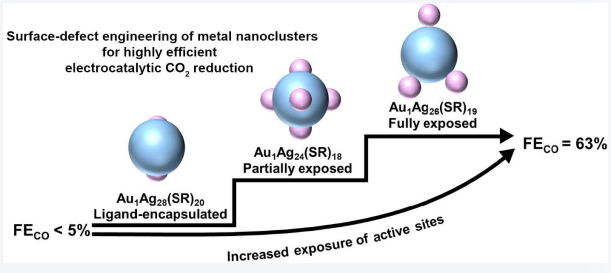

KEYWORDS: metal nanocluster, electrocatalytic CO_2RR, surface-defect engineering, reaction mechanism

1 Introduction

Electrocatalytic carbon dioxide reduction reaction (CO_2RR) is a transformative pathway for simultaneously addressing energy scarcity and environmental challenges [1–3]. However, large-scale implementation of this technology is hindered by two main obstacles: the high thermodynamic stability of CO_2 molecules and the thermodynamically favored hydrogen evolution reaction (HER) [4–7]. To overcome these challenges, it is essential to establish a precise relationship between structure and performance. While traditional metal nanoparticle catalysts provide a high surface area and abundant active sites [8–10], their structural disorder [11, 12], dispersed active sites [13, 14], and insufficient stability [15, 16] make it difficult to identify clear structure-activity correlations. This lack of clarity severely limits the understanding of the mechanisms involved and hampers rational catalyst design. Atomically precise nanoclusters offer a unique opportunity to understand catalytic mechanisms that traditional nanoparticles cannot achieve. Nanoclusters possess precise structures, allowing for a clear establishment of structure-activity relationships, thus enabling the accurate identification of active sites. Furthermore, nanoclusters serve as platforms for surface engineering and performance customization, where their properties can be finely tuned through methods such as ligand exchange or metal doping [17–19]. Finally,

Received: October 29, 2025; **Revised:** January 8, 2026
Accepted: January 10, 2026

✉Address correspondence to Manzhou Zhu, zmz@ahu.edu.cn; Jiangwei Zhang, zjw11@tsinghua.org.cn, jwz@imu.edu.cn; Xi Kang, kangxi_chem@ahu.edu.cn

nanocluster catalysts combine the structural precision of homogeneous catalysts with the recyclability of heterogeneous catalysts, making them an ideal model system for studying the reaction mechanisms of CO_2RR at the atomic scale [20–22].

Previous research indicates that only a small fraction of sites on catalyst surfaces and interfaces act as critical catalytic centers [23]. Consequently, effectively exposing more active sites is essential for improving the catalytic performance of nanoclusters [24, 25]. Defect engineering, which modifies electronic structures and the interfacial microenvironment, can significantly enhance CO_2 activation efficiency and suppress the competing HER [26–28]. This approach serves as a key strategy for optimizing CO_2RR performance. However, in traditional nanoparticle catalysts, structural uncertainties make precise characterization of atomic-level defects challenging [29–31]. Additionally, the disordered nature of defect sites can lead to increased side reactions, such as HER [32, 33]. Structurally precise metal nanoclusters provide an ideal platform to overcome these limitations. Their high structural diversity and rich coordination environments facilitate the construction of structurally analogous nanocluster models, allowing for a systematic investigation of how defect engineering impacts CO_2RR performance [34–39]. For example, He et al. reported that a defective Au_{44}-P catalyst achieved a Faradaic efficiency (FE) of 97% for CO, significantly higher than the 83% FE of its defect-free Au_{44} counterpart; density functional theory calculations revealed that structural defects deviating from the conventional face-centered cubic growth pattern promoted the conversion of CO_2 to CO [40]. The Negishi group constructed two defect-induced Cu_{58} nanoclusters and performed comparative analyses with the structurally regular Cu_{58} nanocluster to assess the influence of surface coordination vacancies and rearrangement of Cu(I) atoms on CO_2RR product selectivity [41]. Nevertheless, current research primarily focuses on the effects of various kernel structures or ligand systems on CO_2RR performance. Therefore, it is imperative to systematically investigate the impact of defect engineering within the nanocluster system that are protected by identical ligands. This strategy effectively eliminates interference from variations in both the kernel structure and the ligand shell, thereby establishing a direct causal relationship between defect structure and catalytic activity.

Here we systematically examined the relationship between structural defects and CO_2RR performance using a series of homologous nanoclusters, $Au_1Ag_{24+2n}(SR)_{18+n}$ (n = 0, 1, 2; SR = adamantanethiol). These clusters share the same icosahedral Au_1Ag_{12} core, but differ in the arrangement of their peripheral stable units. Notably, both Au_1Ag_{26} and Au_1Ag_{28} displayed characteristics of structural defects; however, they exhibited significantly different catalytic behaviors. Electrochemical measurements indicated that at −1.0 V vs. RHE, Au_1Ag_{26} achieved a CO selectivity of 63%, which is nearly double that of Au_1Ag_{24} with a CO selectivity of 32%. In contrast, Au_1Ag_{28} without any surface defect primarily exhibited HER activity. Structural characterization confirmed that this difference in performance stemmed from the way defect engineering influenced the exposure of active sites: the structural defects in Au_1Ag_{26} substantially increased the surface area exposed by metal atoms, while in Au_1Ag_{28}, the surface-active sites were tightly encapsulated by ligands. This finding highlights active site exposure as a crucial factor through which defect engineering can enhance CO_2RR performance, deepening the understanding of structure-activity relationships within homologous nanocluster systems and providing a novel perspective for the rational design of efficient electrocatalysts.

2 Results and discussion

2.1 Construction of nanocluster series

Defect engineering serves as a critical strategy for modulating the performance of the electrocatalytic CO_2RR, yet the atomic-scale structure-activity relationships underlying this approach require urgent elucidation. Our group has previously reported a homologous series of $Au_1Ag_{24+2n}(SR)_{18+n}$ (n = 0, 1, 2) nanoclusters. Possessing identical inner cores and ligands, along with comparable structural frameworks, these clusters serve as ideal model catalysts for establishing the correlation between structural defects and CO_2RR catalytic performance (Fig. 1 and Fig. S1 in the Electronic Supplementary Material (ESM)). Specifically, Au_1Ag_{24}, Au_1Ag_{26}, and Au_1Ag_{28} share the same icosahedral core but differ in their surface-protecting motifs: Au_1Ag_{24} is wrapped by six identical $Ag_2(SR)_3$ motifs, whereas Au_1Ag_{26} is wrapped by three $Ag_2(SR)_3$, one $Ag_3(SR)_4$, and one $Ag_5(SR)_6$ motifs, and Au_1Ag_{28} is wrapped by two $Ag_2(SR)_3$ and two $Ag_6(SR)_7$ motifs (Figs. S2–S5 in the ESM). Consequently, in contrast to Au_1Ag_{24}, which maintains a symmetric distribution of peripheral motifs, Au_1Ag_{26} and Au_1Ag_{28} exhibit symmetry breaking. This structural defect altered the degree of exposure of the active sites, thereby directly affecting the catalytic performance. Space-filling models visually demonstrated distinct surface structural features across the three clusters: Au_1Ag_{24} displays six partially exposed S-Ag_1S_2 units (the solo S is not bonded to Ag_1S_2); Au_1Ag_{26} exposes three asymmetrically distributed Ag_1S_3 units; while in Au_1Ag_{28}, the peripheral motifs completely shield Ag_1S_3 units, leaving only two exposed Ag_2S_1 units. Based on this structural analysis, we hypothesize that the asymmetrically distributed exposed sites on the defective Au_1Ag_{26} surface may enhance CO_2RR performance through strengthened CO_2 adsorption capability. Conversely, Au_1Ag_{28} is anticipated to exhibit significantly reduced CO_2RR activity due to the extensive coverage of its surface sites.

2.2 CO_2RR performance of cluster-based catalysts

To validate these hypotheses, the above nanoclusters were loaded onto activated carbon (AC) support to maintain their catalytic stability, and the CO_2RR performance of the three nanoclusters was tested. To establish a reliable structure–activity relationship, key experimental parameters were strictly controlled. All catalysts were prepared with an identical nanocluster-to-carbon mass ratio of 1:10 using the same amount of nanoclusters (2 mg), ensuring meaningful comparison on an equal-metal basis. Electrode effects were evaluated using catalyst ink volumes of 80, 120, and 160 μL. Au_1Ag_{24} and Au_1Ag_{28} show stable FE_{CO} across all loadings, whereas Au_1Ag_{26} exhibits strong coverage dependence, with FE_{CO} increasing from ~ 30% to ~ 60% at 120 μL and declining at higher loading (Fig. S6 in the ESM). Accordingly, an ink volume of 120 μL was adopted for all subsequent measurements. Transmission electron microscopy (TEM) characterization confirmed that the sizes of all the nanoclusters are within the range of about 1–2 nm and uniformly distributed on the AC support (Fig. S7 in the ESM). The CO_2RR activity of the three catalysts was evaluated via linear sweep voltammetry (LSV) in 0.5 M $KHCO_3$ electrolyte (CO_2-saturated; pH = 7.2). Compared to Au_1Ag_{24}, Au_1Ag_{26} exhibited a significantly enhanced reduction current density, indicating superior CO_2

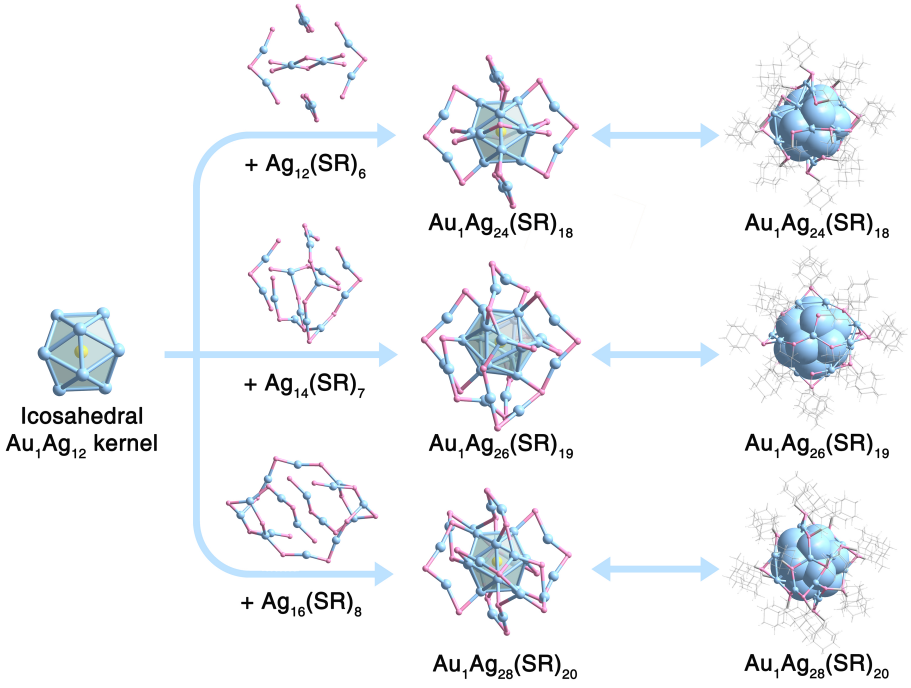

Figure 1 Structural anatomy of $Au_1Ag_{24}(SR)_{18}$, $Au_1Ag_{26}(SR)_{19}$ and $Au_1Ag_{28}(SR)_{20}$ nanoclusters. Color labels: yellow = Au; blue = Ag; pink = S.

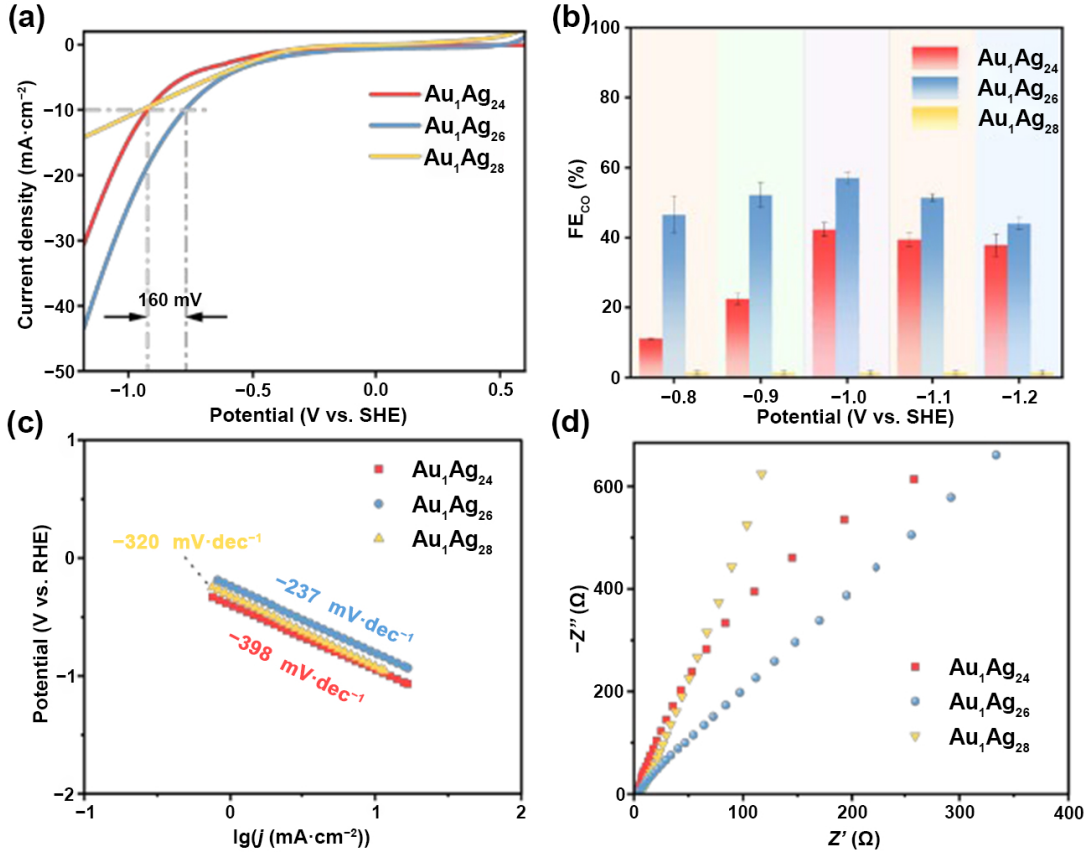

Figure 2 (a) LSV curves of Au_1Ag_{24}, Au_1Ag_{26}, and Au_1Ag_{28} nanoclusters in a CO_2-saturated electrolyte. (b) FE of CO production in electrocatalytic CO_2RR. (c) Tafel slope and (d) electrochemical impedance spectroscopy of Au_1Ag_{24}, Au_1Ag_{26}, and Au_1Ag_{28} nanoclusters.

activation capability (Fig. 2(a)). Conversely, Au_1Ag_{28} showed a substantial decrease in current density, reflecting weakened CO_2 activation. Notably, in the CO_2-saturated electrolyte, Au_1Ag_{26} demonstrated an onset potential 160 mV lower than Au_1Ag_{24}, confirming faster CO_2 reduction reaction kinetics. Qualitative and quantitative analysis of gaseous/liquid products was performed using online gas chromatography (GC) and nuclear magnetic resonance (NMR) spectroscopy (Fig. 2(b)). As a result, within the

entire potential window (−0.8 to −1.2 V), GC detected only CO and H_2, and NMR observed no liquid products. Specifically, Au_1Ag_{24} primarily produced CO (FE_{CO} = 10.2%–40.5%) and H_2. Au_1Ag_{26} exhibited a volcano-shaped CO selectivity profile (FE_{CO} = 45.6%–60.2%), reaching a peak value of 63% at −1.0 V. In contrast, Au_1Ag_{28} generated predominantly H_2 (FE_{H_2} > 95%) over the same potential range, with negligible carbon-containing products. Consequently, the electrocatalytic performance follows the order Au_1Ag_{26} > Au_1Ag_{24} > Au_1Ag_{28}, validating our hypothesis regarding the pivotal role of defect engineering in enhancing CO_2RR performance of cluster-based catalysts.

To elucidate the reasons for the enhanced CO_2RR performance of the Au_1Ag_{26} nanocluster, we first conducted Tafel analysis (Fig. 2(c)). The results revealed that Au_1Ag_{26} exhibited a lower Tafel slope (237 mV·dec^{-1}), significantly lower than that of Au_1Ag_{24} (398 mV·dec^{-1}) and Au_1Ag_{28} (320 mV·dec^{-1}), confirming superior charge transfer kinetics in Au_1Ag_{26}. Electrochemical impedance spectroscopy (EIS) revealed that performance differences stem from electronic transmission efficiency. The identical 45° Warburg region observed for all three nanoclusters suggested that diffusion-controlled processes governed the rate-determining step. The smaller semicircle diameter in Nyquist plots for Au_1Ag_{26} indicates reduced charge transfer resistance (Fig. 2(d)). Furthermore, electrochemical active surface area (ECSA) measurements revealed a higher accessible active site density for Au_1Ag_{26} (Fig. S8 in the ESM). We have conducted extended potentiostatic electrolysis experiments lasting up to 10 h, with sampling for Faradaic efficiency analysis performed at hourly intervals to more accurately assess catalyst stability. The results indicate that, at their optimal potentials, the FE_{CO} of the three catalysts (Au_1Ag_{24}, Au_1Ag_{26} and Au_1Ag_{28}) showed no significant decline during the 10-hour testing, demonstrating good robustness (Fig. S9 in the ESM). This finding preliminarily validates the stability and catalytic durability of our nanocluster catalysts under CO_2RR conditions. The absence of significant particle aggregation was verified by TEM analysis, confirming the structural robustness of these cluster-based catalysts (Fig. S7 in the ESM).

Online differential electrochemical mass spectrometry (DEMS) was employed to investigate the catalytic reaction pathways for the three nanoclusters. Distinct *m/z* signals at 2 and 28 Da, corresponding to H_2 and CO, respectively, were observed during chronoamperometry for both Au_1Ag_{24} and Au_1Ag_{26}, while only the H_2 signal was detected for Au_1Ag_{28} (Figs. 3(a) and 3(b)). Notably, the CO-related signal on Au_1Ag_{26} appeared at a lower potential and exhibited higher peak intensity, indicating more favorable reaction kinetics for CO_2 reduction. *In situ* attenuated total reflection surface-enhanced infrared absorption spectroscopy (ATR-SEIRAS) revealed key reaction intermediates among the CO_2RR. Vibrational signatures at 1234, 1658, 2140, and 3350 cm^{-1} were observed on both Au_1Ag_{24} and Au_1Ag_{26} catalysts (Figs. 3(c) and 3(d)), assigned respectively to: (i) asymmetric stretching vibration of COOH groups, (ii) bending vibration of H_2O molecules, (iii) stretching vibration of the adsorbed CO species, and (iv) O–H stretching vibrations. These identical spectral features confirm a common reaction pathway. Critically, *in situ* ATR-SEIRAS revealed markedly more intense infrared absorption bands on Au_1Ag_{26} compared to Au_1Ag_{24} at equivalent potentials (Fig. S10 in the EMS), providing direct evidence for its superior catalytic performance. Comparative analysis of infrared absorption peak areas revealed that at −1.0 V, the peak intensities for *COOH (1234 cm^{-1}), *OH (3350 cm^{-1}), and *CO (2140 cm^{-1}) intermediates on Au_1Ag_{26} nanoclusters increased by factors of 1.5, 1.8, and 2.8 times, respectively, relative to Au_1Ag_{24} (Fig. 3(e)). Such enhancements correlate with DEMS data,

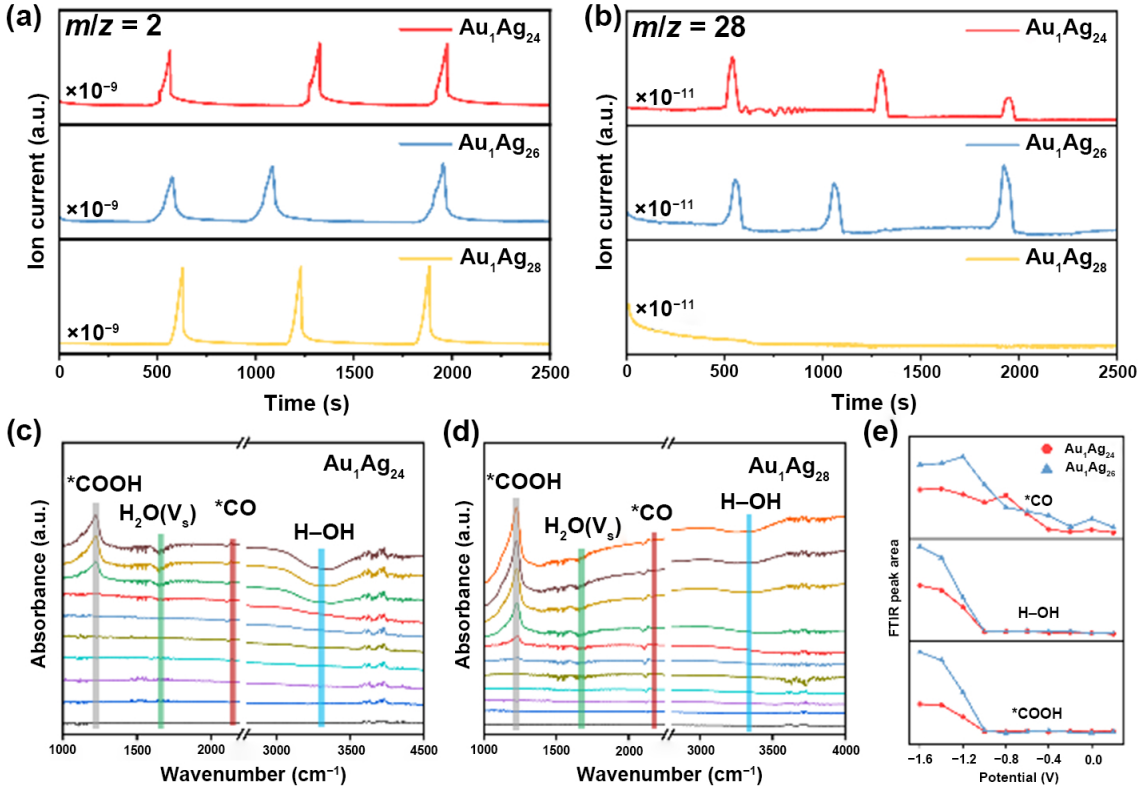

Figure 3 The *m/z* signal of (a) 2 Da and (b) 28 Da in online DEMS over Au_1Ag_{24}, Au_1Ag_{26}, and Au_1Ag_{28} nanoclusters. *In-situ* FTIR spectra of (c) Au_1Ag_{24} and (d) Au_1Ag_{26} nanoclusters at different potentials. (e) Comparison of the *in-situ* infrared absorption peak areas of Au_1Ag_{24} and Au_1Ag_{26} nanoclusters.

collectively demonstrating stronger intermediate adsorption at active sites.

2.3 Correlations between surface defect and CO_2RR activity

Numerous studies have confirmed that defects or asymmetric sites within crystals often act as active centers for catalytic reactions due to their ability to form unsaturated coordination structures or special electronic properties, thereby promoting the adsorption of reactants and stabilizing key intermediates. Single-crystal structural analyses indicate that, compared to the highly symmetric Au_1Ag_{24}, the asymmetric structures Au_1Ag_{26} and Au_1Ag_{28} exhibit more distorted surface morphologies and more complex coordination environments. This is specifically manifested in the transformation of some μ_2-S (sulfur bridges connecting two silver atoms) to μ_3-S (sulfur bridges connecting three silver atoms) (Fig. S11 in the ESM). This symmetry-breaking and reconstruction process induced by defect engineering may further generate more unsaturated coordination sites, serving as potential catalytic active centers [42, 43].

In thiol-protected nanoclusters, CO_2 molecules preferentially interact with surface sulfur atoms through their oxygen atoms, inducing electronic rearrangements and electronic depletion in the sulfur region. Comparisons of XPS spectra before and after electrochemical testing reveal that the binding energy of sulfur increases by approximately 0.7 eV after the reaction, indicating enhanced interaction between the outer electrons and the atomic nucleus, which reflects the electronic modulation role of sulfur sites during the reaction process (Fig. S12 in the ESM). Additionally, in asymmetric structures, the uneven distribution of bond lengths and angles (Fig. S5 in the ESM) enables some sulfur atoms to possess higher localized electron densities or more compatible orbital energy levels, thereby more effectively stabilizing key reaction intermediates such as *COOH and significantly lowering the reaction energy barrier.

Therefore, these active sites can fundamentally be viewed as interface structures constructed through the synergy of metal and sulfur atoms, exemplified by motifs such as Au_1S_3 and Cu_1S_3. This study integrates structural characterization and electrochemical performance analysis to clearly establish the structure-activity relationship between surface defects and the CO_2 reduction reaction (CO_2RR) activity (Figs. 4(a)–4(c)). Importantly, we found that the CO_2RR activity is positively correlated with the extent of the exposed Ag_1S_3 motif on the surface. Structural reconstructions not only enhance the density of these potential active sites but also facilitate the dissociation of water by optimizing the interfacial charge distribution, thereby ensuring efficient proton supply throughout the reaction process. Further comparisons show that the exposed active area of Au_1Ag_{26} is 1.8 times larger than that of Au_1Ag_{24} (Fig. S13 in the ESM), directly corresponding to its superior catalytic performance. In contrast, while Au_1Ag_{24} lacks the Ag_1S_3 motif, the close packing of its neighboring active units can still maintain a certain level of catalytic capability. Conversely, although Au_1Ag_{28} possesses Ag_1S_3 units, its overly dense ligand encapsulation prevents active sites from being accessed, thereby reinforcing the critical role of "site exposure" in catalysis. Moreover, previous studies have demonstrated that thiol doping aids in accelerating water splitting and enhancing proton supply [44–47], further supporting the conclusion in this study regarding "exposed Ag_1S_3 units as catalytic active sites".

Based on the above analysis, we propose a reaction mechanism centered on the Ag_1S_3 active site (Fig. 4(d)): (i) CO_2 adsorption and activation: The CO_2 molecule preferentially adsorbs on the fully exposed Ag_1S_3 unit, forming the key intermediate *CO_2; (ii) protonation to form *COOH: The adsorbed *CO_2 intermediate combines with a proton (H^+) derived from adjacent water molecules to form the *COOH intermediate; (iii) hydrogenation to

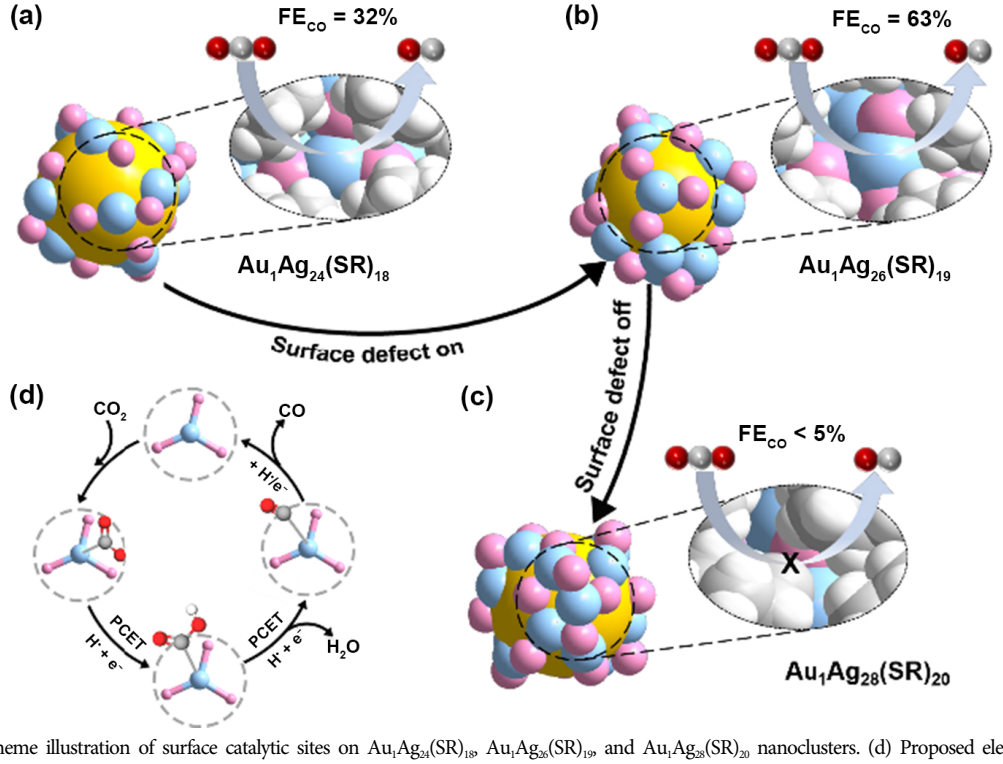

Figure 4 (a)–(c) Scheme illustration of surface catalytic sites on $Au_1Ag_{24}(SR)_{18}$, $Au_1Ag_{26}(SR)_{19}$, and $Au_1Ag_{28}(SR)_{20}$ nanoclusters. (d) Proposed electrocatalytic reaction pathway for converting CO_2 into CO via the Ag_1S_3 surface-active site.

form *CO: The *COOH intermediate undergoes further proton/electron transfer (hydrogenation), converting into the *CO intermediate; (iv) CO desorption: The *CO intermediate eventually desorbs from the Ag_1S_3 active site, releasing the CO gas product. Thus, the overall reaction pathway is proposed as: * + CO_2 → *CO_2 → *COOH → *CO → * + CO.

3 Conclusions

In summary, the $Au_1Ag_{24+2n}(SR)_{18+n}$ (n = 0, 1, 2) nanoclusters series investigated in this study exhibit markedly distinct electrocatalytic performance correlated to their surface defects. Notably, the catalytic CO selectivity of Au_1Ag_{26} (FE_{CO} = 63%) is approximately twice that of Au_1Ag_{24} (FE_{CO} = 32%), while Au_1Ag_{28} exhibits negligible activity. Through comprehensive structural characterization and electrochemical measurements, we identified a strong positive correlation between electrocatalytic performance and the exposure of Ag_1S_3 active motifs on the nanocluster surface. Overall, this research reveals the fundamental mechanism by which structural defects influence the catalytic performance of nanoclusters at the atomic level, primarily by increasing the accessible surface area of active sites. This finding not only deepens the understanding of how defect engineering affects catalytic performance but also establishes a foundational platform for the rational design of efficient CO_2 reduction reaction catalysts.

Electronic Supplementary Material: Supplementary material (Figs. S1–S13 include structural analysis and comparison, TEM images, stability tests, *in situ* infrared spectroscopy comparisons, XPS spectra before and after testing, and a comparison of exposed active-site area) is available in the online version of this article at https://doi.org/10.26599/NR.2026.94908428.

Data availability

All other data are available from the authors upon reasonable request.

Acknowledgements

This project was financially supported by the National Natural Science Foundation of China (Nos. U24A20480, 22371003, 22471001, and U22A20107), the Ministry of Education, Natural Science Foundation of Anhui Province (No. 2408085Y006), the Scientific Research Program of Universities in Anhui Province (No. 2022AH030009), Technology Breakthrough Engineering Hydrogen Energy Field "Unveiling and Leading" Project (No. 2024KJTW0018), Inner Mongolia Autonomous Region Natural Science Foundation (No. 2023MS02002), and the National Key R&D Program of China (No. 2022YFA1205201).

Declaration of competing interest

All the contributing authors report no conflict of interests in this work.

Author contribution statement

X. K., J. W. Z., and M. Z. Z. conceived the idea. H. Q. L., Y. F. W., X. W., R. R., and Z. H. C. performed the synthesis and catalysis. All the authors have approved the final manuscript.

Use of AI statement

None.

References

[1] Yang, P. P.; Gao, M. R. Enrichment of reactants and intermediates for electrocatalytic CO_2 reduction. *Chem. Soc. Rev.* **2023**, *52*, 4343–4380.

[2] Wang, R. T.; Yang, X. K.; Zhang, J. P.; Wen, S. L.; Yan, L. T.; Zhao, X. B.; Guo, E. Y. *In-situ* characterization technologies and theoretical calculations in carbon dioxide reduction: In-depth understanding of reaction mechanisms and rational design of electrocatalysts. *Coord. Chem. Rev.* **2025**, *533*, 216541.

[3] Gonglach, S.; Paul, S.; Haas, M.; Pillwein, F.; Sreejith, S. S.; Barman, S.; De, R.; Müllegger, S.; Gerschel, P.; Apfel, U. P. et al. Molecular cobalt corrole complex for the heterogeneous electrocatalytic reduction of carbon dioxide. *Nat. Commun.* **2019**, *10*, 3864.

[4] Thevenon, A.; Rosas-Hernández, A.; Fontani Herreros, A. M.; Agapie, T.; Peters, J. C. Dramatic HER suppression on Ag electrodes via molecular films for highly selective CO_2 to CO reduction. *ACS Catal.* **2021**, *11*, 4530–4537.

[5] Li, A.; Cao, Q.; Zhou, G. Y.; Schmidt, B. V. K. J.; Zhu, W. J.; Yuan, X. T.; Huo, H. L.; Gong, J. L.; Antonietti, M. Three-phase photocatalysis for the enhanced selectivity and activity of CO_2 reduction on a hydrophobic surface. *Angew. Chem., Int. Ed.* **2019**, *58*, 14549–14555.

[6] Zhou, N. N.; Yin, Y. R.; Luo, B. J.; Fu, Y. X.; Ma, X. X.; Dai, C. Y. Electrocatalytic CO_2 reduction promoted by catalyst-bound proton-abstracting ligands. *Chem. Eng. J.* **2025**, *509*, 161455.

[7] Liu, M. H.; Liu, S. J.; Xu, Q.; Miao, Q. Y.; Yang, S.; Hanson, S.; Chen, G. Z.; He, J.; Jiang, Z.; Zeng, G. F. Dual atomic catalysts from COF-derived carbon for CO_2RR by suppressing HER through synergistic effects. *Carbon Energy* **2023**, *5*, e300.

[8] Jung, H.; Lee, S. Y.; Lee, C. W.; Cho, M. K.; Won, D. H.; Kim, C.; Oh, H. S.; Min, B. K.; Hwang, Y. J. Electrochemical fragmentation of Cu_2O nanoparticles enhancing selective C–C coupling from CO_2 reduction reaction. *J. Am. Chem. Soc.* **2019**, *141*, 4624–4633.

[9] Jeon, H. S.; Sinev, I.; Scholten, F.; Divins, N. J.; Zegkinoglou, I.; Pielsticker, L.; Cuenya, B. R. Operando evolution of the structure and oxidation state of size-controlled Zn nanoparticles during CO_2 electroreduction. *J. Am. Chem. Soc.* **2018**, *140*, 9383–9386.

[10] Woldu, A. R.; Yohannes, A. G.; Huang, Z. L.; Kennepohl, P.; Astruc, D.; Hu, L. S.; Huang, X. C. Experimental and theoretical insights into single atoms, dual atoms, and sub-nanocluster catalysts for electrochemical CO_2 reduction (CO_2RR) to high-value products. *Adv. Mater.* **2024**, *36*, 2414169.

[11] Wu, W. X.; Xu, L. P.; Lu, Q.; Sun, J. P.; Xu, Z. Y.; Song, C. S.; Yu, J. C.; Wang, Y. Addressing the carbonate issue: Electrocatalysts for acidic CO_2 reduction reaction. *Adv. Mater.* **2025**, *37*, 2312894.

[12] Zhai, Y. J.; Han, P.; Yun, Q. B.; Ge, Y. Y.; Zhang, X.; Chen, Y.; Zhang, H. Phase engineering of metal nanocatalysts for electrochemical CO_2 reduction. *eScience* **2022**, *2*, 467–485.

[13] Jia, M. W.; Choi, C.; Wu, T. S.; Ma, C.; Kang, P.; Tao, H. C.; Fan, Q.; Hong, S.; Liu, S. Z.; Soo, Y. L. et al. Carbon-supported Ni nanoparticles for efficient CO_2 electroreduction. *Chem. Sci.* **2018**, *9*, 8775–8780.

[14] Jia, G. R.; Wang, Y.; Sun, M. Z.; Zhang, H.; Li, L. J.; Shi, Y. B.; Zhang, L. Z.; Cui, X. Q.; Lo, T. W. B.; Huang, B. L. et al. Size effects of highly dispersed bismuth nanoparticles on electrocatalytic reduction of carbon dioxide to formic acid. *J. Am. Chem. Soc.* **2023**, *145*, 14133–14142.

[15] Shi, H. J.; Luo, L. L.; Li, C. C.; Li, Y.; Zhang, T. T.; Liu, Z. L.; Cui, J. L.; Gu, L.; Zhang, L.; Hu, Y. J. et al. Stabilizing Cu^+ species in Cu_2O/CuO catalyst via carbon intermediate confinement for selective CO_2RR. *Adv. Funct. Mater.* **2024**, *34*, 2310913.

[16] Okatenko, V.; Castilla-Amorós, L.; Stoian, D. C.; Vávra, J.; Loiudice,

A.; Buonsanti, R. The native oxide skin of liquid metal Ga nanoparticles prevents their rapid coalescence during electrocatalysis. *J. Am. Chem. Soc.* **2022**, *144*, 10053–10063.
[17] Li, Y. W.; Jin, R. C. Seeing ligands on nanoclusters and in their assemblies by X-ray crystallography: Atomically precise nanochemistry and beyond. *J. Am. Chem. Soc.* **2020**, *142*, 13627–13644.
[18] Kang, X.; Li, Y. W.; Zhu, M. Z.; Jin, R. C. Atomically precise alloy nanoclusters: Syntheses, structures, and properties. *Chem. Soc. Rev.* **2020**, *49*, 6443–6514.
[19] Li, Y. W.; Zhou, M.; Jin, R. C. Programmable metal nanoclusters with atomic precision. *Adv. Mater.* **2021**, *33*, 2006591.
[20] Jin, R. C.; Li, G.; Sharma, S.; Li, Y. W.; Du, X. S. Toward active-site tailoring in heterogeneous catalysis by atomically precise metal nanoclusters with crystallographic structures. *Chem. Rev.* **2021**, *121*, 567–648.
[21] Yang, D.; Sun, Y. N.; Cai, X.; Hu, W. G.; Dai, Y. H.; Zhu, Y.; Yang, Y. H. Catalytic conversion of C_1 molecules on atomically precise metal nanoclusters. *CCS Chem.* **2022**, *4*, 66–94.
[22] Du, Y. X.; Sheng, H. T.; Astruc, D.; Zhu, M. Z. Atomically precise noble metal nanoclusters as efficient catalysts: A bridge between structure and properties. *Chem. Rev.* **2020**, *120*, 526–622.
[23] Zhang, H.; Chen, L.; Dong, F.; Lu, Z. W.; Lv, E. M.; Dong, X. L.; Li, H. X.; Yuan, Z. Y.; Peng, X. W.; Yang, S. H. et al. Dynamic transformation of active sites in energy and environmental catalysis. *Energy Environ. Sci.* **2024**, *17*, 6435–6481.
[24] Yang, S.; An, H. Y.; Arnouts, S.; Wang, H.; Yu, X.; de Ruiter, J.; Bals, S.; Altantzis, T.; Weckhuysen, B. M.; van der Stam, W. Halide-guided active site exposure in bismuth electrocatalysts for selective CO_2 conversion into formic acid. *Nat. Catal.* **2023**, *6*, 796–806.
[25] Ma, Y.; Yang, Q.; Qi, J.; Zhang, Y.; Gao, Y. L.; Zeng, Y.; Jiang, N.; Sun, Y.; Qu, K. Q.; Fang, W. H. et al. Surface atom knockout for the active site exposure of alloy catalyst. *Proc. Natl. Acad. Sci. USA* **2024**, *121*, e2319525121.
[26] Muhammad, P.; Zada, A.; Rashid, J.; Hanif, S.; Gao, Y. N.; Li, C. C.; Li, Y. Y.; Fan, K. L.; Wang, Y. L. Defect engineering in nanocatalysts: From design and synthesis to applications. *Adv. Funct. Mater.* **2024**, *34*, 2314686.
[27] Shi, X. S.; Shi, L.; Wang, J. Y.; Zhou, Y.; Zhao, S. L. Defect engineering of nanomaterials for selective electrocatalytic CO_2 reduction. *Matter* **2024**, *7*, 4233–4259.
[28] Wang, Y. F.; Han, P.; Lv, X. M.; Zhang, L. J.; Zheng, G. F. Defect and interface engineering for aqueous electrocatalytic CO_2 reduction. *Joule* **2018**, *2*, 2551–2582.
[29] Kim, I.; Lee, G. B.; Kim, S.; Jung, H. D.; Kim, J. Y.; Lee, T.; Choi, H.; Jo, J.; Kang, G.; Oh, S. H. et al. Unveiling the reconstruction of copper bimetallic catalysts during CO_2 electroreduction. *Nat. Catal.* **2025**, *8*, 697–713.
[30] Zhang, C. R.; Gu, Y. C.; Jiang, Q.; Sheng, Z. Y.; Feng, R. H.; Wang, S. H.; Zhang, H. Y.; Xu, Q. Q.; Yuan, Z. J.; Song, F. Exploration of gas-dependent self-adaptive reconstruction behavior of Cu_2O for electrochemical CO_2 conversion to multi-carbon products. *Nano-Micro Lett.* **2025**, *17*, 66.
[31] Jia, Y. F.; Ding, Y. X.; Song, T.; Xu, Y. L.; Li, Y. Q.; Duan, L. L.; Li, F.; Sun, L. C.; Fan, K. Dynamic surface reconstruction of amphoteric metal (Zn, Al) doped Cu_2O for efficient electrochemical CO_2 reduction to C_{2+} products. *Adv. Sci.* **2023**, *10*, 2303726.
[32] Chen, Y.; Chen, C.; Cao, X. S.; Wang, Z. Y.; Zhang, N.; Liu, T. X. Recent advances in defect and interface engineering for electroreduction of CO_2 and N_2. *Acta Phys. Chim. Sin.* **2023**, *39*, 2212053.
[33] Wang, M. L.; Shi, Z. J.; Shi, W. W.; Jiang, J. Y.; Lan, J. H.; Li, R. Z.; Yan, Y. Y.; Liu, Z. Y.; Fu, L. Y.; Liu, X. G. et al. Ultrafast H-spillover in intermetallic PtZn induced by the local disorder for excellent electrocatalytic hydrogen evolution performance. *Adv. Mater.* **2025**, *37*, 2409575.
[34] Gupta, R. K.; Wang, Z.; Mohan, B.; Tung, C. H.; Sun, D. Atomically precise coinage metal nanoclusters with exposed metal sites: Unlocking reactivity and functionality. *Adv. Funct. Mater.* **2025**, *35*, 2507047.
[35] Ghosh, M.; Sarma, R.; Kamiyama, M.; Kawawaki, T.; Biswas, S.; Negishi, Y. Next-generation CO_2 electroreduction: The role of atomically precise nanoclusters and emerging catalytic strategies. *Nanoscale Horiz.* **2025**, *10*, 1250–1267.
[36] Zhao, J. T.; Ziarati, A.; Bürgi, T. Tuning atomically precise gold nanoclusters for selective electroreduction of CO_2. *Angew. Chem., Int. Ed.* **2025**, *64*, e202504320.
[37] Han, C.; Yang, T.; Fang, Y. Q.; Du, Y. X.; Jin, S.; Xiong, L.; Zhu, M. Z. Steering the product selectivity of CO_2 electroreduction by single atom switching in isostructural copper nanocluster catalysts. *Angew. Chem., Int. Ed.* **2025**, *64*, e202503417.
[38] Su, S. Y.; Zhou, Y. T.; Xiong, L.; Jin, S.; Du, Y. X.; Zhu, M. Z. Structure-activity relationships of the structural analogs Au_8Cu_1 and Au_8Ag_1 in the electrocatalytic CO_2 reduction reaction. *Angew. Chem., Int. Ed.* **2024**, *63*, e202404629.
[39] Tan, Y. S.; Sun, G. L.; Jiang, T. T.; Liu, D.; Li, Q. Z.; Yang, S.; Chai, J. S.; Gao, S.; Yu, H. Z.; Zhu, M. Z. Symmetry breaking enhancing the activity of electrocatalytic CO_2 reduction on an icosahedron-kernel cluster by Cu atoms regulation. *Angew. Chem., Int. Ed.* **2024**, *63*, e202317471.
[40] Zhuang, S. L.; Chen, D.; Ng, W. P.; Liu, L. J.; Sun, M. Y.; Liu, D. Y.; Nawaz, T.; Xia, Q.; Wu, X.; Huang, Y. L. et al. Phosphine-triggered structural defects in Au_{44} homologues boost electrocatalytic CO_2 reduction. *Angew. Chem., Int. Ed.* **2023**, *62*, e202306696.
[41] Biswas, S.; Tanaka, T.; Song, H. H.; Ogami, M.; Shingyouchi, Y.; Hossian, S.; Kamiyama, M.; Kosaka, T.; Nakatani, R.; Niihori, Y. et al. Highly selective methanol synthesis using electrochemical CO_2 reduction with defect-engineered Cu_{58} nanoclusters. *Small Sci.* **2025**, *5*, 2570007.
[42] Mei, Z. W.; Chen, K. J.; Tan, Y.; Liu, Q. W.; Chen, Q.; Wang, Q. Y.; Wang, X. Q.; Cai, C.; Liu, K.; Fu, J. W. et al. Proton feeding from defect-rich carbon support to cobalt phthalocyanine for efficient CO_2 electroreduction. *Chin. J. Catal.* **2024**, *62*, 190–197.
[43] Zhang, H. Q.; Wang, X. X.; Chen, C.; Yang, X. F.; Dong, C.; Huang, Y. C.; Zhao, X. L.; Yang, D. J. Selective CO_2-to-formic acid electrochemical conversion by modulating electronic environment of copper phthalocyanine with defective graphene. *Chin. J. Struct. Chem.* **2023**, *42*, 100089.
[44] Chen, W. M.; Che, Y. X.; Xia, J.; Zheng, L. R.; Lv, H. F.; Zhang, J.; Liang, H. W.; Meng, X. M.; Ma, D.; Song, W. G. et al. Metal-sulfur interfaces as the primary active sites for catalytic hydrogenations. *J. Am. Chem. Soc.* **2024**, *146*, 11542–11552.
[45] Chen, S. Y.; Li, X. Q.; Kao, C. W.; Luo, T.; Chen, K. J.; Fu, J. W.; Ma, C.; Li, H. M.; Li, M.; Chan, T. S. et al. Unveiling the proton-feeding effect in sulfur-doped Fe–N–C single-atom catalyst for enhanced CO_2 electroreduction. *Angew. Chem., Int. Ed.* **2022**, *61*, e202206233.
[46] Yin, P.; Luo, X.; Ma, Y. F.; Chu, S. Q.; Chen, S.; Zheng, X. S.; Lu, J. L.; Wu, X. J.; Liang, H. W. Sulfur stabilizing metal nanoclusters on carbon at high temperatures. *Nat. Commun.* **2021**, *12*, 3135.
[47] Ma, W. C.; Xie, S. J.; Zhang, X. G.; Sun, F. F.; Kang, J. C.; Jiang, Z.; Zhang, Q. H.; Wu, D. Y.; Wang, Y. Promoting electrocatalytic CO_2 reduction to formate via sulfur-boosting water activation on indium surfaces. *Nat. Commun.* **2019**, *10*, 892.